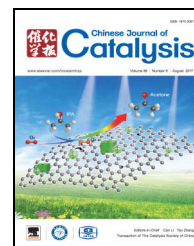


available at [www.sciencedirect.com](http://www.sciencedirect.com)journal homepage: [www.elsevier.com/locate/chnjc](http://www.elsevier.com/locate/chnjc)

## Article

# Peroxymonosulfate activation by $Mn_3O_4$ /metal-organic framework for degradation of refractory aqueous organic pollutant rhodamine B

Longxing Hu <sup>a,\*</sup>, Guihua Deng <sup>a</sup>, Wencong Lu <sup>b</sup>, Yongsheng Lu <sup>a</sup>, Yuyao Zhang <sup>a</sup><sup>a</sup> School of Environmental and Chemical Engineering, Shanghai University, Shanghai 200444, China<sup>b</sup> College of Sciences, Shanghai University, Shanghai 200444, China

## ARTICLE INFO

## Article history:

Received 26 April 2017

Accepted 19 June 2017

Published 5 August 2017

## Keywords:

Peroxymonosulfate activation

Refractory organic pollutant

Degradation

Metal-organic framework

 $Mn_3O_4$ /ZIF-8

## ABSTRACT

An environmentally friendly Mn-oxide-supported metal-organic framework (MOF),  $Mn_3O_4$ /ZIF-8, was successfully prepared using a facile solvothermal method, with a formation mechanism proposed. The composite was characterized using X-ray diffraction, scanning electron microscopy, transmission electron microscopy, X-ray photoelectron microscopy, and Fourier-transform infrared spectroscopy. After characterization, the MOF was used to activate peroxymonosulfate (PMS) for degradation of the refractory pollutant rhodamine B (RhB) in water. The composite prepared at a 0.5:1 mass ratio of  $Mn_3O_4$  to ZIF-8 possessed the highest catalytic activity with negligible Mn leaching. The maximum RhB degradation of approximately 98% was achieved at 0.4 g/L 0.5-Mn/ZIF-120, 0.3 g/L PMS, and 10 mg/L initial RhB concentration at a reaction temperature of 23 °C. The RhB degradation followed first-order kinetics and was accelerated with increased 0.5-Mn/ZIF-120 and PMS dosages, decreased initial RhB concentration, and increased reaction temperature. Moreover, quenching tests indicated that  $\bullet OH$  was the predominant radical involved in the RhB degradation; the  $\bullet OH$  mainly originated from  $SO_4^{\bullet -}$  and, hence, PMS.  $Mn_3O_4$ /ZIF-8 also displayed good reusability for RhB degradation in the presence of PMS over five runs, with a RhB degradation efficiency of more than 96% and Mn leaching of less than 5% for each run. Based on these findings, a RhB degradation mechanism was proposed.

© 2017, Dalian Institute of Chemical Physics, Chinese Academy of Sciences.

Published by Elsevier B.V. All rights reserved.

## 1. Introduction

Refractory organic pollutants originate from different industries [1] and can remain in the environment for a long time after their discharge. Because of the toxicity, carcinogenicity, mutagenicity, and teratogenicity of refractory organic pollutants, their presence in effluents may pose a great threat to human health and aquatic life, even at low levels [2]. Advanced oxidation processes (AOPs) have emerged as efficient processes for the complete degradation of organic compounds in

aqueous media. These processes are based on the in situ generation of highly reactive radicals, such as the hydroxyl radical ( $OH\bullet$ ),  $O_2^{\bullet -}$ ,  $OOH\bullet$ , and the sulfate radical ( $SO_4^{\bullet -}$ ), for mineralization of refractory organic pollutants [3–7]. Although the  $OH\bullet$ -involved AOPs (e.g., Fenton reaction) are well established and widely used,  $SO_4^{\bullet -}$ -involved AOPs have received increasing attention because of their advantages over the former [8–12]. For the generation of  $SO_4^{\bullet -}$ , peroxymonosulfate (PMS, a component of Oxone) is recognized as the most common commercially available oxidant and is also an environmentally friendly

\* Corresponding author. Tel/Fax: +86-21-66137771; E-mail: [hulxhbb@shu.edu.cn](mailto:hulxhbb@shu.edu.cn)

This work was supported by the National Key Research and Development Program of China (2016YFB0700504).

DOI: 10.1016/S1872-2067(17)62875-4 | <http://www.sciencedirect.com/science/journal/18722067> | Chin. J. Catal., Vol. 38, No. 8, August 2017

reagent [13]. The generation of  $\text{SO}_4^{\bullet-}$  from PMS can be achieved via several routes, such as thermal treatment [14], ultraviolet (UV) irradiation [15], sonication [16], and utilization of catalysts [17–19]; however, the use of catalysts appears to be the most feasible route [20]. Various catalysts, such as bases [21], transition metals [22,23], zero-valent metals [24,25], and metal-free materials [26], have been developed to activate PMS. Transition metals have been shown to be the most efficient catalysts, with Co ions specifically serving as the best catalysts [27]. However, neither homogeneous  $\text{Co}^{2+}$ /PMS nor heterogeneous Co-supported catalysts can completely avoid the loss or leaching of Co ions, which thus leads to secondary heavy-metal pollution [26,28]. Therefore, for environmental remediation, there is a strong need to develop novel efficient catalysts to activate PMS without the associated leaching of toxic metals.

Thus far, Mn oxides have attracted considerable attention as heterogeneous catalysts [29–33], adsorbents [34,35], and battery materials [36–38] because these oxides, including MnO,  $\text{MnO}_2$ ,  $\text{Mn}_2\text{O}_3$ , and  $\text{Mn}_3\text{O}_4$ , are abundant on earth, almost non-toxic to the ecosystem, and possess a redox cycle between +2, +3, and +4 valences. Wang's group [39] fabricated Mn oxides in different oxidation states and used them for activating PMS for phenol degradation; they observed the following catalytic activity sequence:  $\text{Mn}_2\text{O}_3 > \text{MnO} > \text{Mn}_3\text{O}_4 > \text{MnO}_2$ . Despite the high catalytic activity of single Mn oxide particles, especially nanoparticles, the extreme fineness of the oxides tends to cause particle aggregation into the bulk, thus depressing the catalytic activity and limiting their practical application. To overcome this difficulty, Mn-oxide-supported materials have been investigated. Han et al. [40] reported that  $\text{Mn}_3\text{O}_4$ -supported SBA-15 exhibited high activity for ethanol degradation in the presence of  $\text{H}_2\text{O}_2$ . In addition,  $\text{Mn}_3\text{O}_4$ -reduced graphene oxide hybrids have been fabricated and applied in the PMS-activated decomposition of Orange II, displaying higher activity than single  $\text{Mn}_3\text{O}_4$  [41]. Similar composites involved in AOPs include graphene oxide/ $\text{Mn}_3\text{O}_4$  [42] and graphene/ $\text{MnO}_2$  [43], where the aggregation of Mn oxide nanoparticles was efficiently reduced. In addition,  $\text{Al}_2\text{O}_3$  [44],  $\text{SiO}_2$  [45],  $\text{ZrO}_2$  [46],  $\text{Fe}_3\text{O}_4$  [47,48], and  $\text{TiO}_2$  [49] have also been used as supports for hybridization with Mn oxides, displaying the specific properties of catalysts, adsorbents, or electrode materials.

Metal-organic frameworks (MOFs) have received considerable attention for catalytic application because of their large surface area, uniform but tunable cavity, and tailorable chemistry [50–52]. Zeolitic imidazolate frameworks (ZIFs) are a subclass of MOFs with zeolite-type topology and outstanding thermal and chemical stabilities [53]. To date, a number of ZIFs with rich structural and topological diversity have been prepared by virtue of the flexibility of the metal and link variation [54]. Compared with SBA-15 [55], graphene oxide [42],  $\text{Fe}_3\text{O}_4$  [47], and  $\text{ZrO}_2$  [46], which require high energy consumption during preparation or complicated synthesis procedures, ZIFs are much easier to prepare with mild reaction conditions. Some studies have demonstrated the use of ZIFs and ZIF-derived materials as heterogeneous catalysts for activating PMS. For instance, Lin's group [56] reported for the first time that ZIF-67 (a Co-based MOF) could efficiently activate PMS to degrade

rhodamine B (RhB) in water. They also reported several MOF-derived materials for activating PMS to degrade RhB, acid yellow, and caffeine in water [57–59]. One of the ZIFs with sodalite topology, ZIF-8 ( $\text{Zn}(\text{C}_4\text{H}_5\text{N}_2)_2$ ) with a molecular weight of 227 g/mol, cavity of 11.6 Å, and pore aperture of 3.4 Å [60], has attracted considerable attention because its hydrothermal stability is better than those of other MOFs. Au, Ag, Pd, and Ru nanoparticles have been supported on ZIF-8 using different processes, and the resulting structures have been applied in catalytic reactions other than PMS activation [61–63]. Additionally, some metal oxide ( $\text{ZnO}$ ,  $\text{TiO}_2$ , etc.)-supported ZIF-8 structures acting as photocatalysts to degrade methylene blue or RhB have also been investigated [64,65]. Nevertheless, to the best of our knowledge, there have been no investigations on the preparation of  $\text{Mn}_3\text{O}_4$ /MOFs or their applications.

RhB is a carcinogenic, toxic, and highly water-soluble xanthene organic compound with a complex structure and high stability that is widely used in various industries, resulting in a recognized refractory-organic-pollutant-containing effluent [66,67]. The major techniques employed to remove RhB from water include adsorption [2], photocatalytic oxidation [68], the Fenton process [69], ultrasonic degradation [70], ozonation [71], and electrochemical oxidation [72]. Adsorption is easy to achieve with a high removal efficiency; however, this process only transfers the pollutants from the liquid to solid phase, resulting in secondary pollution. Other techniques require special equipment or devices or high energy consumption, resulting in high capital and operating costs. The Fenton process is a rapid and inexpensive process; however, it has several significant disadvantages such as the acidic pH (pH = 2–4), production of large amounts of iron sludge, and low total organic carbon removal efficiency.

In this study, an environmentally friendly composite,  $\text{Mn}_3\text{O}_4$ /ZIF-8, was first prepared by a solvothermal method and then utilized for the PMS-activated degradation of RhB in aqueous solutions. The effects of the preparation conditions on the catalyst performance and of several reaction parameters on the catalytic degradation of RhB were examined. Furthermore, a mechanism for the catalyst preparation and RhB degradation was proposed, and the regeneration and reusability of the composite were investigated.

## 2. Experimental

### 2.1. Materials

Zinc nitrate hexahydrate ( $\text{Zn}(\text{NO}_3)_2 \cdot 6\text{H}_2\text{O}$ ), 2-methylimidazole ( $\text{C}_4\text{H}_6\text{N}_2$ , 2-HMIM), sodium formate ( $\text{NaCOOH} \cdot 2\text{H}_2\text{O}$ ), *N,N*-dimethylformamide (DMF), potassium permanganate ( $\text{KMnO}_4$ ), sodium nitrite ( $\text{NaNO}_2$ ), methanol (MeOH), ethanol (EtOH), and *tert*-butyl alcohol (TBA) were purchased from Sinopharm Chemical Reagent Co., Ltd. Oxone ( $2\text{KHSO}_5 \cdot \text{KHSO}_4 \cdot \text{K}_2\text{SO}_4$ ,  $\text{KHSO}_5$ , with PMS as an active component) was purchased from Shanghai Future Chemical Technology Co., Ltd. All the reagents were used as-received without further purification. Deionized water was used throughout the investigation.

## 2.2. Preparation of ZIF-8, Mn<sub>3</sub>O<sub>4</sub>, and Mn<sub>3</sub>O<sub>4</sub>/ZIF-8

### 2.2.1. Preparation of ZIF-8

ZIF-8 was prepared using a previously reported facile room-temperature colloidal chemistry route with modifications [73–75]; sodium formate was used to enhance the heterogeneous nucleation and intergrowth of ZIF-8 crystals [76]. A typical synthesis is described as follows. Zn(NO<sub>3</sub>)<sub>2</sub>·6H<sub>2</sub>O (8.77 g) was dissolved in 50 mL of DMF, and 9.20 g NaCOOH·2H<sub>2</sub>O and 9.68 g 2-HMIM were mixed and dissolved in 25 mL of DMF. Then, the former solution was added to the latter. The molar ratio of the final growth solution was 1:4:3:33 (Zn(NO<sub>3</sub>)<sub>2</sub>·6H<sub>2</sub>O:2-HMIM:NaCOOH·2H<sub>2</sub>O:DMF). The solution turned milky after several minutes and was stirred at room temperature for 4 h for ZIF-8 growth. The resulting solid products were recovered by centrifugation at 3000 r/min for 5 min. Once separated, they were alternatively resuspended in methanol and deionized water for rinsing and centrifugation. This operation was repeated 5–6 times; finally, the solid materials were dried in air at 70 °C overnight.

### 2.2.2. Preparation of Mn<sub>3</sub>O<sub>4</sub>

Mn<sub>3</sub>O<sub>4</sub> samples were prepared using the facile solvothermal method reported by Zhang et al. [77] with some modifications. Briefly, 1.04 g KMnO<sub>4</sub> was dissolved in 120 mL of aqueous ethanol (60%) at room temperature to form a homogeneous solution. The solution was then transferred into a 200-mL Teflon-lined stainless steel autoclave and heated at 120 °C for 8 h. After naturally cooling to room temperature, the resulting precipitates were recovered by centrifugation, washed with deionized water, and finally dried in air at 70 °C overnight.

### 2.2.3. Preparation of Mn<sub>3</sub>O<sub>4</sub>/ZIF-8

We successfully prepared Mn<sub>3</sub>O<sub>4</sub>/ZIF-8 as a novel composite. In a typical synthesis, 0.50 g of the prepared ZIF-8 was dispersed into 120 mL of aqueous ethanol (60%) with stirring for 1 h. Then, 1.04 g KMnO<sub>4</sub> was added to the suspension, which was magnetically stirred for 1 h to ensure that the KMnO<sub>4</sub> was completely dissolved. Next, the mixture was transferred into a 200-mL Teflon-lined stainless steel autoclave, which was sealed and heated to 120 °C. After incubation for 8 h, the autoclave was naturally cooled to room temperature. The resulting precipitates were separated by centrifugation, washed with deionized water, and finally dried in air at 70 °C overnight. The prepared sample was labeled 0.5-Mn/ZIF-120.

By modifying the ZIF-8 and KMnO<sub>4</sub> dosages and the solvothermal temperature, we obtained different Mn<sub>3</sub>O<sub>4</sub>/ZIF-8 composites, which were labeled *n*-Mn/ZIF-120, where *n* represents the Mn<sub>3</sub>O<sub>4</sub> loading on ZIF-8 (mass ratio of Mn<sub>3</sub>O<sub>4</sub> to ZIF-8), with values of 0.25, 0.5, 1.0, and 1.5.

For comparison, a mechanical mixture of ZIF-8 and Mn<sub>3</sub>O<sub>4</sub> was also prepared and was labeled Mn<sub>3</sub>O<sub>4</sub>+ZIF.

## 2.3. Characterization

X-ray diffraction (XRD) patterns of the samples were obtained using a Rigaku D/Max-2200X powder X-ray diffractom-

eter with a Cu K<sub>α</sub> radiation source of wavelength 1.54056 Å at 40 kV and 40 mA. The wide-angle data were collected from 5° to 80° (2θ) with a scan speed of 8°/min. The external morphologies of the samples were examined using scanning electron microscopy (SEM; JEOL JSM-6700F). The internal structures of the samples were characterized using high-resolution transmission electron microscopy (HRTEM; JEOL JEM-2010F) with a field-emission gun at 200 kV. The surface element compositions and chemical states of the samples were analyzed using X-ray photoelectron spectroscopy (XPS; ESCALAB 250Xi) with 300-W Al K<sub>α</sub> radiation. Fourier-transform infrared (FT-IR) spectra were recorded from KBr pellets in the range of 4000–400 cm<sup>-1</sup> on a Nicolet 6700 spectrometer.

## 2.4. Degradation tests

The catalytic activities of the prepared materials were evaluated based on the degradation of RhB in aqueous solutions at room temperature. The RhB degradation tests were performed in an 800-mL glass reactor containing 500 mL of the RhB solutions. The reactants were stirred at 4000 r/min. Unless specifically stated, the reaction temperature was maintained at 23 °C, with an initial solution pH of 5.18 and RhB concentration of 10 mg/L. In a typical test, a fixed amount of catalyst was added to the RhB solution and stirred for 30 min to achieve adsorption–desorption equilibrium; then, a known amount of PMS was added to the reactor to initiate the degradation. At fixed intervals, 6-mL samples of the suspension were removed with a syringe and quenched with excess sodium nitrite to prevent further reaction. The suspensions were separated by centrifugation at 3000 r/min for 5 min to obtain the supernatant for subsequent analysis.

For the catalyst recyclability tests, the used solid material was recovered by filtration, washed with deionized water, and then dried in an oven at 70 °C for 12 h before the next use. Several parallel tests were conducted for every run before the last run to ensure that there was sufficient catalyst for the next run.

## 2.5. Analytical methods

The RhB concentrations were quantified using a ultraviolet-visible (UV-vis) spectrophotometer (UV-5300PC, Shanghai) at 552 nm. The Mn concentration in the aqueous solution was measured using inductively coupled plasma (ICP) emission spectrometry (Prodigy). UV-vis spectra were obtained using a UV-vis spectrophotometer (UV-5300PC, Shanghai) at different reaction times, with the spectra scanned from 300 to 650 nm. The principal degradation products of RhB were detected by gas chromatography-mass spectrometry (GC-MS) using an Agilent 7890A gas chromatograph equipped with an HP-5 MS capillary column (30 m × 0.25 mm × 0.25 μm) combined with an Agilent 5975C mass spectrometer. For the gas chromatography, the injection temperature was 250 °C; the initial temperature of 70 °C was maintained for 2 min and increased to 300 °C at a heating rate of 20 °C/min, which was maintained for another 6 min; the flow rate of He was 1 mL/min; and the sample injected was 1 μL. For the mass spectrometry, an HP-5 MS

capillary column was used, along with electrospray ionization and an ionizing energy of 70 eV, scanning range of 41–450 amu, and ion source and transmission line temperatures of 250 °C.

The tests were generally conducted in duplicate, and the experimental errors were all below 3%.

### 3. Results and discussion

#### 3.1. Characterization of ZIF-8 and $Mn_3O_4$ /ZIF-8

##### 3.1.1. XRD

The crystal structures of the synthesized ZIF-8 and  $Mn_3O_4$ /ZIF-8 composites were determined using powder XRD analysis. As observed in Fig. 1(a), the characteristic peaks of the as-synthesized ZIF-8 matched very well with the simulated ZIF-8 pattern, indicating that the sample consisted of a single ZIF-8 phase [54]. Fig. 1(b) displays the XRD patterns of the  $n$ -Mn/ZIF-120 composites with different  $Mn_3O_4$  loadings. The characteristic peaks of both  $Mn_3O_4$  and ZIF-8 were detected in the composite samples, implying that  $Mn_3O_4$  was successfully dispersed onto the surface of ZIF-8 without destruction of the ZIF-8 structure, verifying the high hydrothermal stability of ZIF-8 during the synthesis process. With increasing  $Mn_3O_4$  loading, the intensities of the  $Mn_3O_4$  peaks increased, demonstrating the improved crystallinity with higher  $Mn_3O_4$  loading. Moreover, no additional peaks were detected, suggesting the high purity of the  $Mn_3O_4$ /ZIF-8 composites as end products.

##### 3.1.2. SEM and TEM

SEM images of the prepared samples are presented in Fig. 2(a) and (b). The 0.5-Mn/ZIF-120 sample exhibited a cauliflower-like surface morphology, and  $Mn_3O_4$  sheets with sizes ranging from a few tens to hundreds of nanometers were observed on the surface of ZIF-8. The average particle size of ZIF-8 was approximately 250 nm. To obtain insight into the structure of the 0.5-Mn/ZIF-120 composite, TEM and HRTEM images were obtained, as shown in Fig. 2(c) and (d). Fig. 2(c) clearly shows that the  $Mn_3O_4$  nanoparticles with sizes of

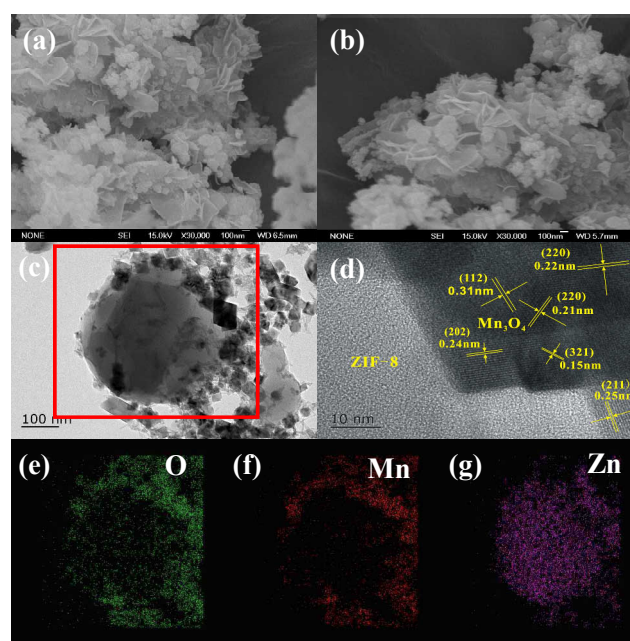


**Fig. 2.** SEM (a,b), TEM (c), and HRTEM (d) images of as-synthesized 0.5-Mn/ZIF-120 composite. EDX mapping images of O (e), Mn (f), and Zn (g) for the sample in (c).

50–150 nm were closely deposited on the surface of ZIF-8. Fig. 2(d) presents an HRTEM image of the 0.5-Mn/ZIF-120 composite with well-defined lattice fringes, which indicates that the  $Mn_3O_4$  nanoparticles were highly crystallized. The lattice spacings were approximately 0.31, 0.25, 0.24, 0.22 and 0.15 nm, corresponding to the (112), (211), (202), (220) and (321) planes of  $Mn_3O_4$  (JCPDS No. 24-0734), respectively, which is in accordance with the XRD results. No evidence of the presence of  $Mn_3O_4$  inside the ZIF-8 was observed in any of the TEM images. Fig. 2(e)–(g) presents energy-dispersive X-ray spectrometry (EDX) elemental mappings of Fig. 2(c). Most of the Mn was located in the outer layer of the sample, whereas Zn was mainly concentrated in the core region, indicating the dispersion of

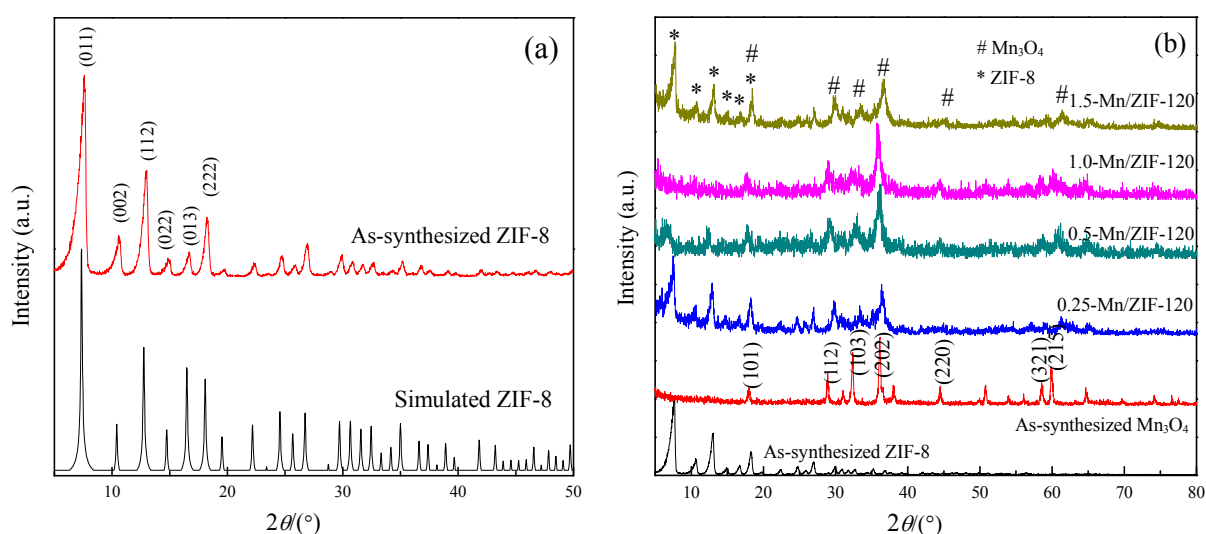


**Fig. 1.** XRD patterns of ZIF-8 (a) and  $Mn_3O_4$ /ZIF-8 (b) composites.

Mn<sub>3</sub>O<sub>4</sub> nanoparticles on the external surface of ZIF-8 instead of in its internal structure.

### 3.1.3. XPS

To understand the composition and chemical bonding of the 0.5-Mn/ZIF-120 composite, XPS measurements were performed (Fig. 3). Strong peaks of Mn 2*p*, Zn 2*p*, C 1*s*, N 1*s*, and O 1*s* are observed in Fig. 3(a). In the Mn 2*p* region (Fig. 3(b)), two peaks are observed at binding energies of 641.5 and 652.9 eV, which correspond to the Mn 2*p*<sub>1/2</sub> and Mn 2*p*<sub>3/2</sub> levels, respectively, and the splitting width (11.4 eV) is consistent with a previous report on Mn<sub>3</sub>O<sub>4</sub> [78]. The Mn 2*p*<sub>3/2</sub> peak could be further divided into two peaks. The peak at 640.6 eV was assigned to the Mn 2*p*<sub>3/2</sub> peak of MnO and the other peak at 641.8 eV coincided with the Mn 2*p*<sub>3/2</sub> peak of Mn<sub>2</sub>O<sub>3</sub>. Based on the peak areas, Mn(II) and Mn(III) accounted for 37.82 and 62.18 of the total Mn<sub>3</sub>O<sub>4</sub> supported on ZIF-8, respectively. In the Zn 2*p* profile (Fig. 3(c)), two peaks are observed at 1020.8 (Zn 2*p*<sub>3/2</sub>) and 1044.0 eV (Zn 2*p*<sub>1/2</sub>), which are compatible with Zn<sup>2+</sup> of the ZIF-8 structure [79]. In the C 1*s* region, three peaks are observed: the carbon peak at lower binding energy, 284.4 eV, is consistent with adventitious carbon, which accumulates on nearly all samples exposed to air [80], and the carbon peaks at 284.9 and 286.0 eV are attributed to the presence of methyl imidazole groups and carbonates, respectively [81,82]. Moreover, by fitting the N 1*s* region (Fig. 3(e)), two peaks were obtained: the main peak at 398.7 eV and a smaller peak at 399.9 eV, which were assigned to the imidazole groups and uncoordinated methyl imidazole linkers [81–83], respectively. For oxygen (Fig. 3(f)), three different peaks located at 529.3, 530.7, and 531.9 eV, respectively, were observed, which correspond

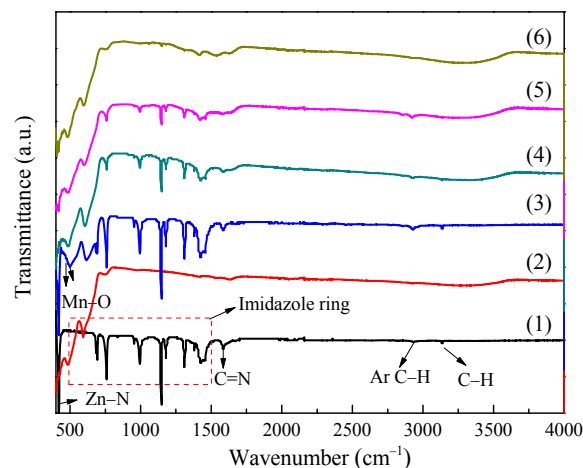


**Fig. 4.** FT-IR spectra of as-prepared composites. (1) ZIF-8; (2) Mn<sub>3</sub>O<sub>4</sub>; (3) 0.25-Mn/ZIF-120; (4) 0.5-Mn/ZIF-120; (5) 1.0-Mn/ZIF-120; (6) 1.5-Mn/ZIF-120.

to Mn–O–Mn, Zn–O, and carbonates in the Mn<sub>3</sub>O<sub>4</sub>/ZIF-8 composite, respectively [81]. The XPS analyses are in good agreement with the XRD results.

### 3.1.4. FT-IR

To further identify the molecular structure and functional groups of the as-synthesized ZIF-8 and *n*-Mn/ZIF-120, FT-IR spectra were recorded, and the results are presented in Fig. 4. For ZIF-8, the peak at 420 cm<sup>-1</sup> is attributed to the Zn–N stretching mode. In addition, the peaks in the 500–1350 and 1350–1500 cm<sup>-1</sup> spectral regions can be assigned as plane bending and stretching of the imidazole ring, respectively.

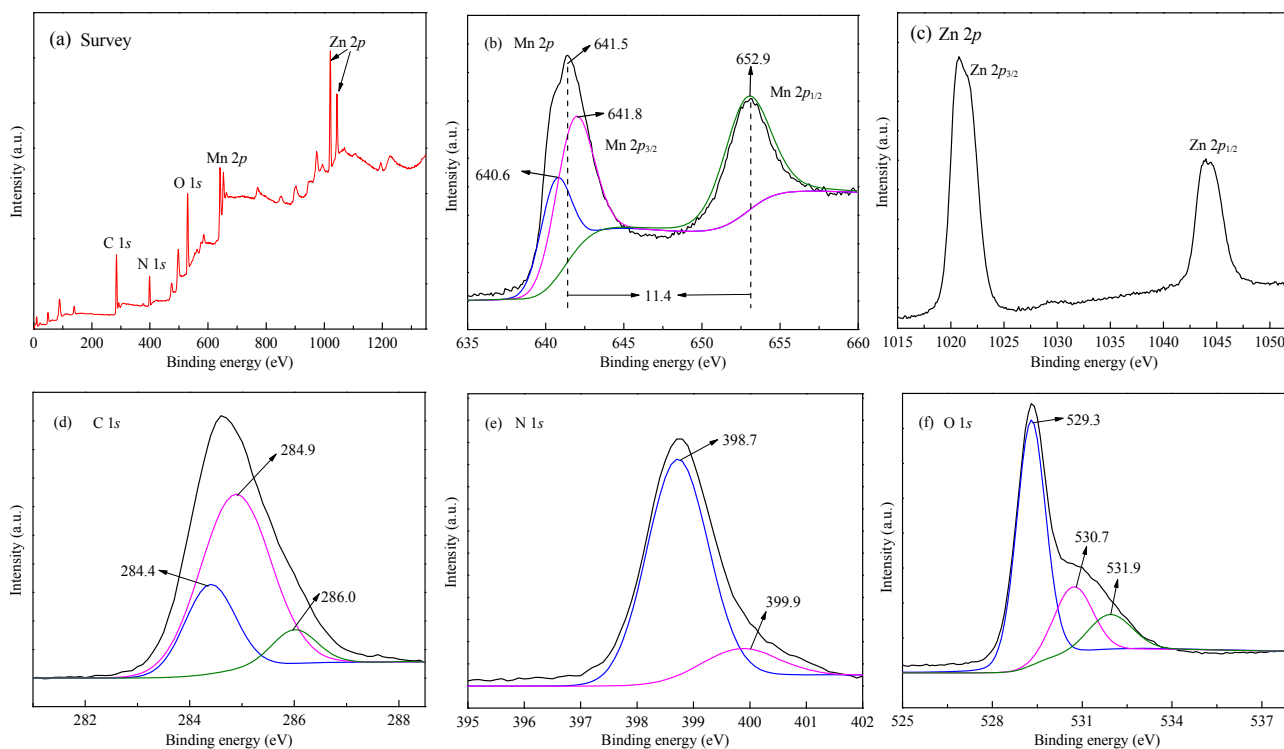
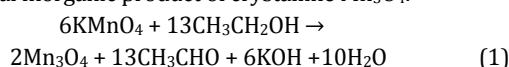


**Fig. 3.** XPS spectra of as-synthesized 0.5-Mn/ZIF-120 composite.

Peaks for the C=N stretching mode at 1580  $\text{cm}^{-1}$  and for the aromatic and aliphatic C-H stretching at 2930 and 3140  $\text{cm}^{-1}$  are also observed [84]. Two new peaks appeared for the *n*-Mn/ZIF-120 composites at 494 and 484  $\text{cm}^{-1}$ , representing the vibration of the Mn-O stretching modes of tetrahedral and octahedral sites, respectively. In addition, in the FT-IR spectra of the *n*-Mn/ZIF-120 composites with different  $\text{Mn}_3\text{O}_4$  loadings, the diffractions of both ZIF-8 and  $\text{Mn}_3\text{O}_4$  can be detected. These results support the formation of a  $\text{Mn}_3\text{O}_4$ /ZIF-8 structure.

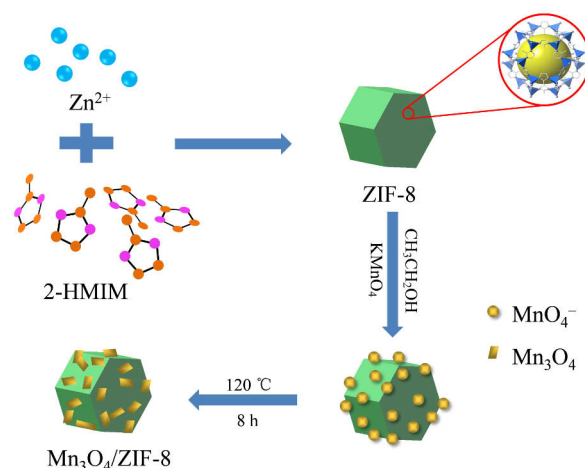
### 3.1.5. Formation mechanism of $\text{Mn}_3\text{O}_4$ /ZIF-8

Based on the preparation procedures and characterization of the  $\text{Mn}_3\text{O}_4$ /ZIF-8 composites, the  $\text{Mn}_3\text{O}_4$ /ZIF-8 preparation route is presented in Scheme 1. First, ZIF-8 was synthesized at room temperature by dispersing  $\text{Zn}(\text{NO}_3)_2 \cdot 6\text{H}_2\text{O}$  in DMF and 2-HMIM and  $\text{NaCOOH} \cdot 2\text{H}_2\text{O}$  in DMF and then mixing the two solutions together, resulting in the formation of ZnO, which acted as a heterogeneous nucleation site as well as a secondary metal source. Once the ZIF crystals were nucleated,  $\text{NaCOOH}$  served as a deprotonator, promoting the intergrowth of ZIF crystals [85]. Second, *n*-Mn/ZIF-120 composites with different  $\text{Mn}_3\text{O}_4$  loadings were fabricated using a solvothermal process, where the prepared ZIF-8 was first dispersed in 60% EtOH solution to create a suspension. Then, a certain amount of  $\text{KMnO}_4$  was dissolved in the suspension to release  $\text{MnO}_4^-$ , which was able to coordinate the  $\text{Zn}^{2+}$  ions in ZIF-8 through electrostatic interaction. During the solvothermal reaction,  $\text{MnO}_4^-$  was reduced by EtOH as described in Eq. (1) [86], which led to the final inorganic product of crystalline  $\text{Mn}_3\text{O}_4$ .



### 3.2. Effect of $\text{Mn}_3\text{O}_4$ loading on performance of $\text{Mn}_3\text{O}_4$ /ZIF-8

The catalytic activity and stability of the prepared *n*-Mn/ZIF-120 composites were evaluated based on the RhB degradation and Mn leaching in solutions in the presence of PMS, respectively. Fig. 5 shows the effect of the  $\text{Mn}_3\text{O}_4$  loading in *n*-Mn/ZIF-120 on the RhB degradation and Mn leaching. As



Scheme 1. Schematic illustration of preparation of  $\text{Mn}_3\text{O}_4$ /ZIF-8.

observed in Fig. 5(a), the effect of  $\text{Mn}_3\text{O}_4$  loading on the RhB degradation was significant, with the RhB degradation efficiency increasing with increasing  $\text{Mn}_3\text{O}_4$  loading from 0.25 to 0.5 and then slightly decreasing with further increase of the  $\text{Mn}_3\text{O}_4$  loading to 1.0. The optimal RhB degradation of 99.4% was achieved in 60 min at 0.5  $\text{Mn}_3\text{O}_4$  loading. However, further increase of the  $\text{Mn}_3\text{O}_4$  loading led to a decreased RhB degradation efficiency because of the “covering effect”; that is, loading of a large amount of  $\text{Mn}_3\text{O}_4$  onto ZIF-8 can result in heavy coverage of the active sites on the support surface. The Mn leaching results are presented in Fig. 5(b); upon increasing the  $\text{Mn}_3\text{O}_4$  loading from 0.25 to 1.0, the Mn leaching slightly increased and then significantly increased at higher loadings. Thus, 0.5-Mn/ZIF-120 is regarded as the best catalyst to achieve the highest RhB degradation with the least Mn leaching and, thus, the highest catalytic activity and stability.

### 3.3. Effect of reaction variables on RhB degradation

#### 3.3.1. Control experiment

The removal of RhB based on adsorption with ZIF-8 and 0.5-Mn/ZIF-120, single chemical oxidation with PMS, and cata-

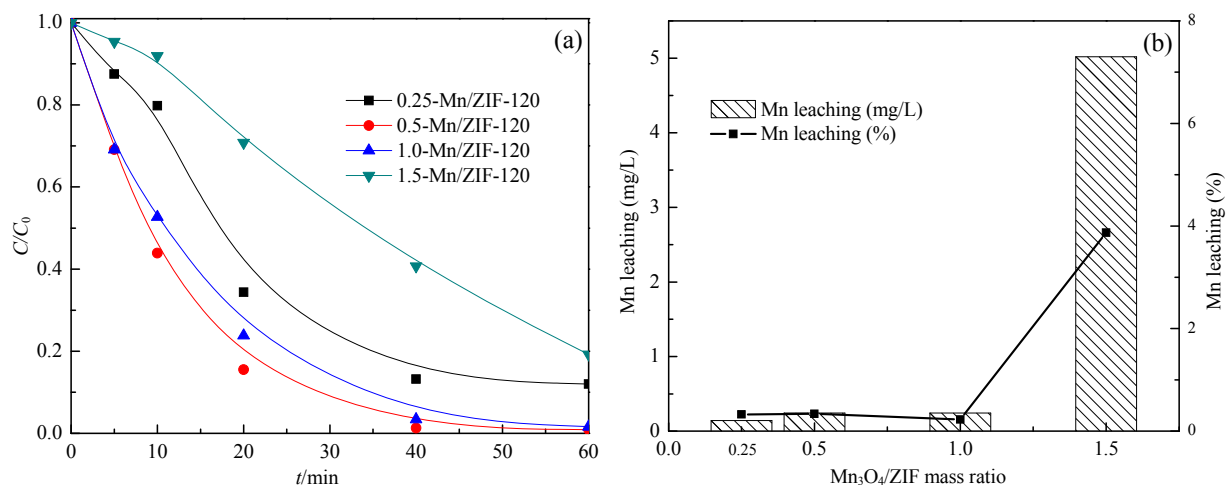


Fig. 5. Effect of  $\text{Mn}_3\text{O}_4$  loading on RhB degradation (a) and Mn leaching (b). Reaction conditions: catalyst dosage 0.3 g/L, RhB 10 mg/L, PMS 0.3 g/L, pH = 5.18 (unadjusted), 23 °C.

lytic degradation with different catalysts in the presence of PMS were evaluated, and the results are presented in Fig. 6. In the single chemical oxidation, the degradation of RhB in 60 min was less than 20%, suggesting that PMS alone cannot efficiently oxidize RhB. Moreover, 0.5-Mn/ZIF-120 and ZIF-8 showed very limited adsorption for RhB. For the RhB catalytic degradation in the presence of PMS with 0.5-Mn/ZIF-120,  $\text{Mn}_3\text{O}_4$ , ZIF-8, and the mixture of  $\text{Mn}_3\text{O}_4$  and ZIF-8 ( $\text{Mn}_3\text{O}_4$ +ZIF), 0.5-Mn/ZIF-120 exhibited the best catalytic activity with almost complete RhB degradation in 60 min. Meanwhile, the RhB degradation in the presence of ZIF-8 and PMS was greater than that in the presence of PMS alone, possibly because of the extra contribution of adsorption by ZIF-8. Notably, the  $\text{Mn}_3\text{O}_4$ +ZIF mixture contributed approximately 65% of the RhB degradation in the presence of PMS in 60 min, less than that contributed by  $\text{Mn}_3\text{O}_4$ , which may be due to PMS consumption by porous ZIF-8 adsorption.

### 3.3.2. Effect of 0.5-Mn/ZIF-120 dosage

Fig. 7 shows the effect of various 0.5-Mn/ZIF-120 dosages on RhB degradation in the presence of PMS. As observed in Fig. 7(a), the RhB degradation efficiency increased with increasing 0.5-Mn/ZIF-120 dosage. Almost complete degradation of RhB was achieved in 60 min for the 0.3 g/L of 0.5-Mn/ZIF-120 dosage. The inset in Fig. 7(b) presents the kinetic curves of RhB degradation, illustrating that the RhB catalytic degradation follows a first-order kinetics model  $\ln C/C_0 = -kt$ , where  $C$  and  $C_0$  represent the RhB concentration at time ( $t$ ) and  $t = 0$ , respectively, and  $k$  ( $\text{min}^{-1}$ ) is the apparent reaction rate constant. As observed in Fig. 7(b), when the 0.5-Mn/ZIF-120 dosage increased from 0.1 to 0.4 g/L,  $k$  increased almost linearly from 0.0367 to 0.1520  $\text{min}^{-1}$ , which can be attributed to the increased numbers of adsorption sites for RhB and active sites for activation of PMS and, hence, more  $\text{SO}_4^{\bullet-}$ .

### 3.3.3. Effect of PMS dosage

The catalytic degradation of RhB was also affected by the PMS dosage, as shown in Fig. 8. The RhB degradation efficiency significantly increased with increasing PMS dosage from 0.1 to

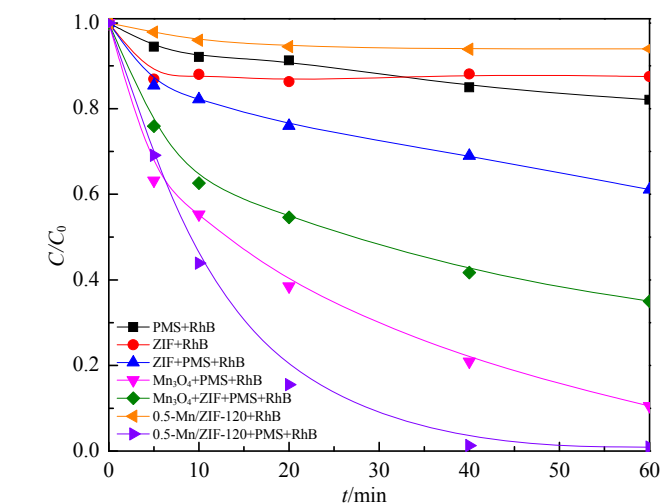
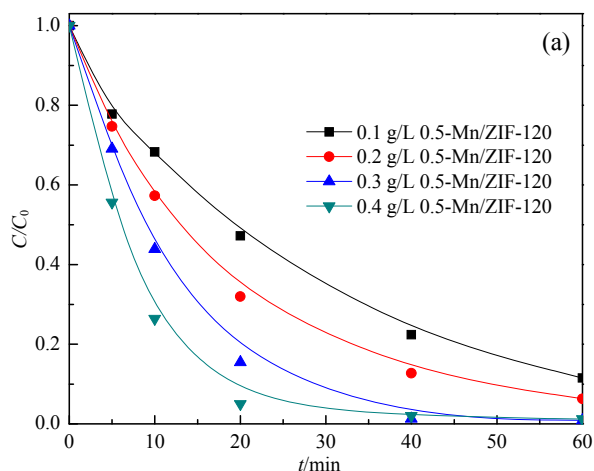


Fig. 6. Removal of RhB in aqueous solutions under various conditions. Reaction conditions: 0.5-Mn/ZIF-120 0.3 g/L,  $\text{Mn}_3\text{O}_4$  0.1 g/L, ZIF-8 0.2 g/L, RhB 10 mg/L, PMS 0.3 g/L, pH = 5.18 (unadjusted), 23 °C.

0.3 g/L and only slightly changed at higher PMS dosages. Fig. 8(b) shows the corresponding relationship between the initial rate constant  $k$  and PMS dosage, with the inset presenting the kinetic fitting curves. The RhB degradation clearly fits the first-order kinetics model well. As observed in Fig. 8, the RhB degradation efficiency and degradation rate constant both increased first and then decreased with further increased PMS dosage. With increasing PMS dosage from 0.1 to 0.5 g/L, the RhB degradation efficiency in 40 min increased from 25% to 92%. Because PMS is the source of the reactive sulfate radicals, the increase of the PMS dosage promotes the generation of sulfate radicals and, hence, faster RhB degradation. However, because of the self-quenching of sulfate radicals by PMS, as indicated in Eq. (2), a further increase of the PMS dosage leads to lower RhB degradation rates [87].



### 3.3.4. Effect of initial RhB concentration

Fig. 9 shows the effect of various initial RhB concentrations

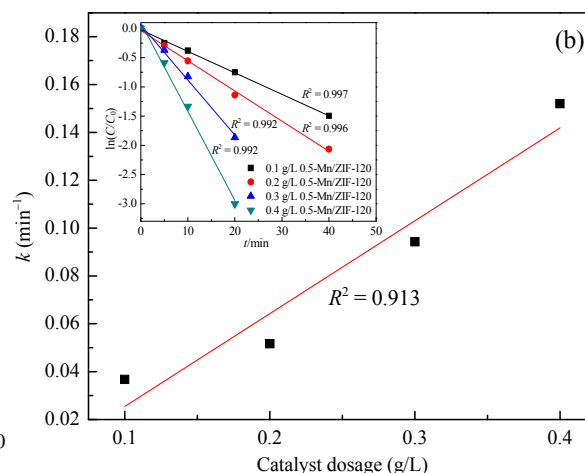
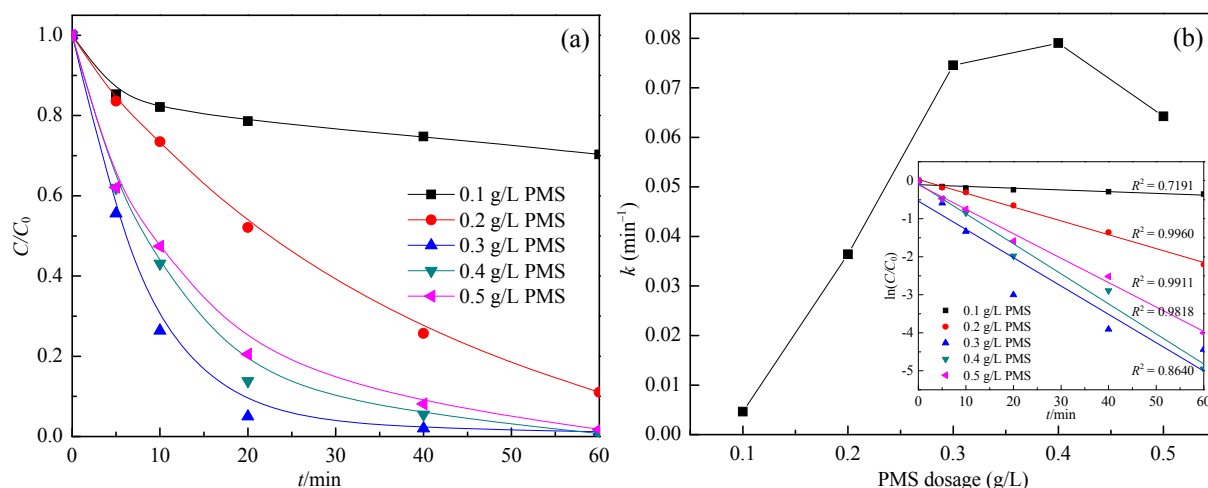
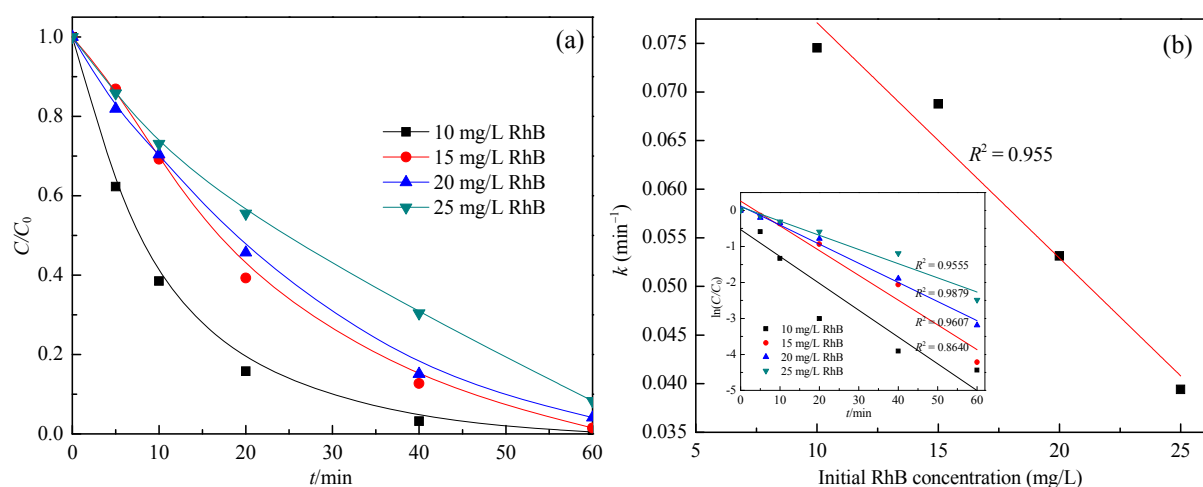


Fig. 7. Effect of 0.5-Mn/ZIF-120 dosage on RhB degradation (a) and its kinetics (b). Reaction conditions: RhB 10 mg/L, PMS 0.3 g/L, pH = 5.18 (unadjusted), 23 °C.



**Fig. 8.** Effect of PMS dosage on RhB degradation (a) and its kinetics (b). Reaction conditions: 0.5-Mn/ZIF-120 0.4 g/L, RhB 10 mg/L, pH = 5.18 (unadjusted), 23 °C.



**Fig. 9.** Effect of initial RhB concentration on RhB degradation (a) and its kinetics (b). Reaction conditions: 0.5-Mn/ZIF-120 0.4 g/L, PMS 0.3 g/L, pH = 5.18 (unadjusted), 23 °C.

on the RhB degradation and degradation kinetics in the presence of 0.5-Mn/ZIF-120 and PMS. As observed in Fig. 9(a), the RhB degradation efficiency decreased with increasing initial RhB concentration. The inset in Fig. 9(b) presents the kinetic curves for RhB degradation, demonstrating that RhB degradation obeys a first-order kinetics model with respect to the substrate RhB. As observed in Fig. 9(b), the kinetic rate constant linearly decreased from 0.0745 to 0.0394 min<sup>-1</sup> with increasing initial RhB concentration from 10 to 25 mg/L. The increase in the initial RhB concentration led to the adsorption of an increased number of RhB molecules on the surface of 0.5-Mn/ZIF-120 and the production of many intermediates and carbonaceous deposits on the catalyst surface during RhB degradation. The RhB degradation in the presence of 0.5-Mn/ZIF-120 and PMS was dependent on the sulfate radicals generated. Because the concentrations of the catalyst and oxidant were the same, the sulfate radical concentrations produced in solution were the same. Therefore, for a higher concentration of RhB in the solution, a longer degradation time was needed [88]. A few researchers have drawn a similar con-

clusion that a higher dye concentration results in greater suppression of dye removal [39,89,90].

### 3.3.5. Effect of reaction temperature

The RhB degradation in the presence of 0.5-Mn/ZIF-120 and PMS under different reaction temperatures is shown in Fig. 10. At room temperature (23 °C), the complete degradation of RhB was achieved in 40 min, whereas at 45 °C, almost complete degradation of RhB was achieved in 20 min, indicating that the RhB degradation by 0.5-Mn/ZIF-120-activated PMS is an endothermic reaction and can be substantially accelerated at elevated temperature [57]. Because the kinetic rate constant  $k$  increased with increasing temperature, the relationship between  $k$  and temperature can be correlated using the Arrhenius equation presented in Eq. (3):

$$\ln k = \ln A - E_a/RT \quad (3)$$

where  $A$  is the pre-exponential factor (min<sup>-1</sup>),  $R$  is the universal gas constant,  $E_a$  is the activation energy, and  $T$  is temperature in Kelvin (K). A plot of  $\ln k$  versus  $1/T$  is presented in the inset of Fig. 10, with the data points perfectly fit by linear regression

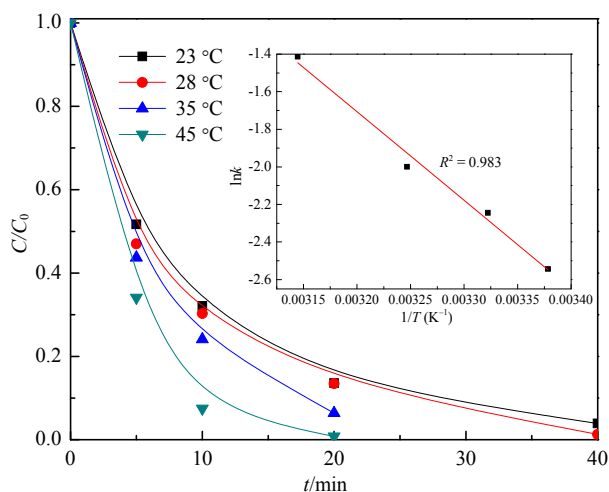


**Fig. 10.** Effect of reaction temperature on RhB degradation and estimation of activation energy. Reaction conditions: 0.5-Mn/ZIF-120 0.4 g/L, RhB 10 mg/L, PMS 0.3 g/L, pH = 5.18 (unadjusted).

with  $R^2$  of 0.983. This finding indicates that  $k$  can be closely associated with temperature by the Arrhenius equation and that  $k$  at other temperatures can be predicted.

Using the Arrhenius equation, the activation energy of the degradation reaction was calculated to be 39.17 kJ/mol. Various reaction activation energies have been reported for Mn-based catalysts used for activating PMS to degrade organics, and these findings are summarized in Table 1. The RhB degradation reaction by 0.5-Mn/ZIF-8-activated PMS has a lower activation energy (and hence a more rapid reaction rate) than those of the reactions initiated by most other Mn-based catalysts.

### 3.4. RhB degradation mechanism

#### 3.4.1. Quenching tests

The activation of PMS by metal-containing catalysts generates two major reactive radicals,  $\text{SO}_4^{\bullet-}$  and  $\text{HO}^{\bullet}$  [93]. To identify the principal radicals for the proposed degradation mechanism, the effect of radical scavengers on RhB catalytic degradation was examined, and the results are presented in Fig. 11. Various quenchers including EtOH and TBA were used. EtOH with alpha hydrogen can readily react with  $\text{SO}_4^{\bullet-}$  and  $\text{HO}^{\bullet}$ , whereas TBA without alpha hydrogen is inert to  $\text{SO}_4^{\bullet-}$  and mainly reacts with  $\text{HO}^{\bullet}$  [94]. As observed in Fig. 11, the RhB degradation profile without the addition of a quencher differed significantly from the profiles with the addition of EtOH or TBA

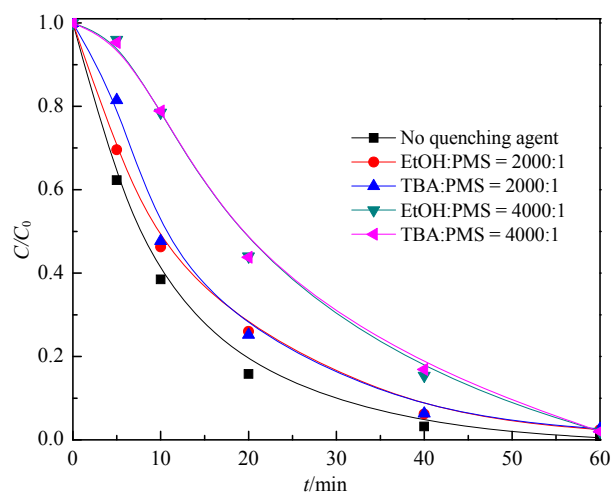
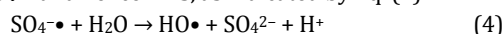


**Fig. 11.** Quenching tests using various radical scavengers. Reaction conditions: 0.5-Mn/ZIF-120 0.4 g/L, RhB 10 mg/L, PMS 0.3 g/L, pH = 5.18 (unadjusted), 23 °C.

at molar ratios of EtOH:PMS or TBA:PMS of 2000:1 or 4000:1. Moreover, little difference between the two degradation profiles was observed with the addition of EtOH or TBA. The RhB degradation in 20 min in the absence of a quencher reached approximately 86.4%, whereas those with the addition of EtOH or TBA at the above molar ratios decreased to approximately 74% and 56%, respectively, suggesting that EtOH and TBA indeed functioned as quenchers during the reaction. Accordingly, it can be concluded that both  $\text{SO}_4^{\bullet-}$  and  $\text{HO}^{\bullet}$  are involved in the attack of RhB in aqueous solutions; however,  $\text{HO}^{\bullet}$  is the predominant active species. Nevertheless,  $\text{HO}^{\bullet}$  is mainly derived from  $\text{SO}_4^{\bullet-}$  and hence PMS, as indicated by Eq. (4).



#### 3.4.2. UV-vis spectra of RhB catalytic degradation

Fig. 12 shows the temporal absorption spectrum changes of RhB degradation by 0.5-Mn/ZIF-120-activated PMS. It is generally accepted that two competitive processes exist for RhB

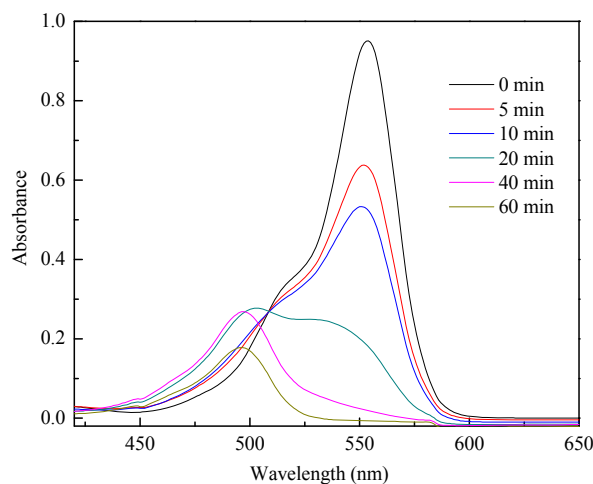


**Fig. 12.** UV-vis absorption spectra of RhB degradation in the presence of 0.5-Mn/ZIF-120 and PMS. Reaction conditions: 0.5-Mn/ZIF-120 0.4 g/L, RhB 10 mg/L, PMS 0.3 g/L, pH = 5.18 (unadjusted), 23 °C.

**Table 1**  
Comparison of activation energies in Mn-based catalysis.

Catalyst	Organics	Activation energy (kJ/mol)	Ref.
$\text{Mn}_3\text{O}_4$ -rGO	Orange II	49.5	[41]
Mn/MCS	Phenol	59.5	[91]
$\text{Mn}_2\text{O}_3$ cubic	Phenol	61.2	[89]
$\alpha$ - $\text{MnO}_2$ nanowire	Phenol	21.9	[88]
Corolla-like $\delta$ - $\text{MnO}_2$	Phenol	25.3	[92]
$\text{Mn}_3\text{O}_4$ /ZIF-8	RhB	39.17	this work

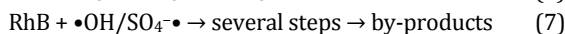
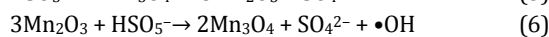
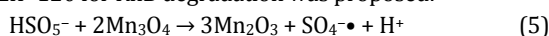
degradation: N-de-ethylation and the destruction of the conjugated structure [95,96]. The intensity of the characteristic peak of RhB at 552 nm clearly decreased to half of its original value in 10 min, indicating the destruction of the conjugated xan-thene structure. In addition, a blue shift of the maximum absorption band of the solution was observed because of the formation of a series of N-de-ethylated intermediates. Thus, it can be deduced that the ring opening simultaneously occurred with N-de-ethylation during the RhB degradation process.

### 3.4.3. Pathway of RhB catalytic degradation

GC-MS analysis of the supernatant phase is very useful for obtaining information about the degradation products. Before the GC-MS analysis, sample derivatization of the resultant solution coupled with extraction with organic solvent methylene chloride was performed. The total ion chromatogram (TIC) spectrum and GC-MS analysis results of the principal degradation by-products of the 0.5-Mn/ZIF-120-PMS-RhB<sub>aq</sub> system are presented in Fig. 13 and Table 2, respectively. The degradation products could be divided into two groups: aromatic compounds with different substituents and organics with lower molecular weights, most of which consisted of organic acid and alcohol. Among the degradation products, the glycerol content was the highest, implying that the conjugated structure of RhB was destroyed and decomposed into simple organics, which could be further converted into CO<sub>2</sub> and H<sub>2</sub>O.

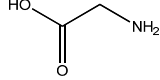
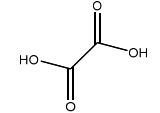
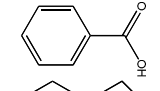
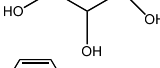
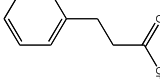
### 3.4.4. Reaction mechanism of RhB degradation by 0.5-Mn/ZIF-120-activated PMS

Based on previous investigations [97] and the quenching test results, the following mechanism of PMS activation by 0.5-Mn/ZIF-120 for RhB degradation was proposed:



First, the activation of PMS by 0.5-Mn/ZIF-120 occurs to generate SO<sub>4</sub><sup>•-</sup> and •OH (Eqs. (5) and (6)), and most of the produced SO<sub>4</sub><sup>•-</sup> radicals are rapidly depleted by reacting with RhB. During the reaction, the generated •OH radicals also attack RhB but at a moderate reaction rate (Eq. (7)). Simultane-

**Table 2**  
Principal by-products of RhB degradation detected by GC-MS.

Time (min)	Identified by-products	Formula
4.53	Ethylene glycol	
4.63	Glycine	
4.98	Ethanedioic acid	
6.82	Benzoic acid	
6.98	Glycerol	
8.02	3-Phenylpropanoic acid	

ously, some of the produced SO<sub>4</sub><sup>•-</sup> radicals react with H<sub>2</sub>O via Eq. (4) to generate •OH. After the depletion of SO<sub>4</sub><sup>•-</sup>, •OH becomes the single reactive species to attack RhB. Meanwhile, the Mn<sub>2</sub>O<sub>3</sub> reacts with PMS, resulting in the regeneration of the original Mn<sub>3</sub>O<sub>4</sub> and •OH (Eq. (6)). Based on these comprehensive considerations, it is suggested that the hydroxyl radicals generated in the presence of 0.5-Mn/ZIF-120 and PMS play a key role in the RhB degradation.

### 3.5. Reusability of Mn<sub>3</sub>O<sub>4</sub>/ZIF-8

The reusability of a catalyst is an important factor reflecting its performance and potential for practical application. The as-synthesized catalyst Mn<sub>3</sub>O<sub>4</sub>/ZIF-8 was easily separated from aqueous solution using simple filtration with a 0.22-μm membrane and regenerated by washing with deionized water three times and then drying in an oven at 60 °C overnight. Fig. 14(a) and (b) show the catalytic activity and corresponding Mn leaching of the reused catalyst, respectively. The catalytic activity of 0.5-Mn/ZIF-120 remained high for five runs, with a RhB degradation efficiency of more than 96% and Mn leaching of less than 5%, indicating the good reusability of the catalyst. In addition, no significant changes were observed in the XRD patterns of the catalyst before and after use (Fig. 14(c)), indicating no significant crystal structure changes of the recycled catalyst.

## 4. Conclusions

A Mn-oxide-supported MOFs material, Mn<sub>3</sub>O<sub>4</sub>/ZIF-8, was successfully synthesized using a facile solvothermal method for the first time. This material was characterized using several techniques and tested for its ability to activate PMS for the degradation of RhB in aqueous solutions. The Mn<sub>3</sub>O<sub>4</sub>/ZIF-8 composite prepared with a Mn<sub>3</sub>O<sub>4</sub>:ZIF-8 mass ratio of 0.5 to 1 exhibited the best catalytic activity and negligible Mn leaching. In addition, the RhB degradation reached 98% in 40 min under the following conditions: 0.4 g/L catalyst dosage, 0.3 g/L PMS

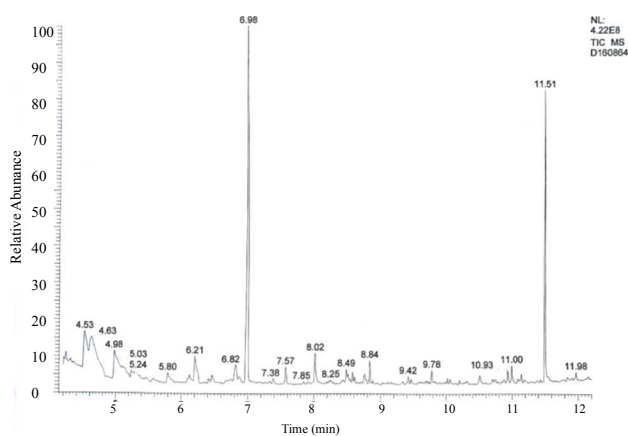


**Fig. 13.** TIC chromatographic spectrum of degradation by-products of RhB.

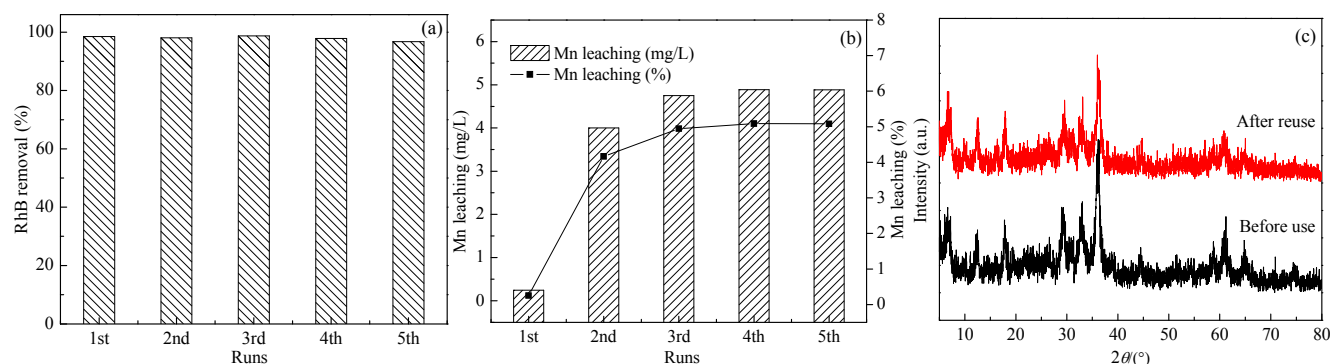


**Fig. 14.** Recycling performance (a) and Mn leaching (b) of 0.5-Mn/ZIF-120 over five runs. XRD patterns (c) of 0.5-Mn/ZIF-120 before and after use. Reaction conditions: 0.5-Mn/ZIF-120 0.4 g/L, RhB 10 mg/L, PMS 0.3 g/L, pH = 5.18 (unadjusted), 23 °C.

dosage, 10 mg/L initial RhB concentration, unadjusted initial solution pH (5.18), and reaction temperature of 23 °C. The catalytic oxidative degradation of RhB in the 0.5-Mn/ZIF-120-PMS system obeyed first-order kinetics, and the degradation rate increased with increasing 0.5-Mn/ZIF-120 and PMS dosages and reaction temperature and decreasing initial RhB concentration. Quenching tests demonstrated that the  $\bullet\text{OH}$  radicals primarily derived from  $\text{SO}_4\text{-}\bullet$  (and hence PMS) were the predominant active radicals attacking RhB. Finally, the catalyst 0.5-Mn/ZIF-120 was effectively recovered and reused for activating PMS to degrade RhB in water for at least five runs.

### Acknowledgments

The characterization of prepared samples was supported by the Analytical and Testing Center of Shanghai University, Shanghai, China.

### References

- [1] D. Shahidi, R. Roy, A. Azzouz, *Appl. Catal. B*, **2015**, 174–175, 277–292.
- [2] Y. R. Wang, W. Chu, *Ind. Eng. Chem. Res.*, **2011**, 50, 8734–8741.
- [3] S. Malato, J. Blanco, C. Richter, B. Braun, M. I. Maldonado, *Appl. Catal. B*, **1998**, 17, 347–356.
- [4] E. Chamarro, A. Marco, S. Esplugas, *Water Res.*, **2001**, 35, 1047–1051.
- [5] G. P. Anipsitakis, D. D. Dionysiou, M. A. Gonzalez, *Environ. Sci. Technol.*, **2006**, 40, 1000–1007.
- [6] M. M. Cheng, W. H. Ma, J. Li, Y. P. Huang, J. Zhao, *Environ. Sci. Technol.*, **2004**, 38, 1569–1575.
- [7] X. Y. Chen, J. W. Chen, X. L. Qiao, D. G. Wang, X. Y. Cai, *Appl. Catal. B*, **2008**, 80, 116–121.
- [8] P. Neta, R. E. Huie, A. B. Ross, *J. Phys. Chem. Ref. Data*, **1988**, 17, 1027–1227.
- [9] M. G. Antoniou, A. A. de la Cruz, D. D. Dionysiou, *Appl. Catal. B*, **2010**, 96, 290–298.
- [10] T. Olmez-Hanci, I. Arslan-Alaton, *Chem. Eng. J.*, **2013**, 224, 10–16.
- [11] E. G. Janzen, Y. Kotake, R. D. Hinton, *Free Radical Biol. Med.*, **1992**, 12, 169–173.
- [12] R. Luo, C. Liu, J. S. Li, J. Wang, X. R. Hu, X. Y. Sun, J. Y. Shen, W. Q. Han, L. J. Wang, *J. Hazard. Mater.*, **2017**, 329, 92–101.
- [13] P. D. Hu, M. C. Long, *Appl. Catal. B*, **2016**, 181, 103–117.
- [14] C. Q. Tan, N. Y. Gao, Y. Deng, N. An, J. Deng, *Chem. Eng. J.*, **2012**, 203, 294–300.
- [15] C. Z. Cui, L. Jin, J. Li, Q. Han, K. F. Lin, S. G. Lu, D. Zhang, G. Cao, *Sci. Total Environ.*, **2016**, 572, 244–251.
- [16] A. B. Kurukutla, P. S. S. Kumar, S. Anandan, T. Sivasankar, *Environ. Eng. Sci.*, **2015**, 32, 129–140.
- [17] K. H. Chan, W. Chu, *Water Res.*, **2009**, 43, 2513–2521.
- [18] Y. R. Wang, W. Chu, *J. Hazard. Mater.*, **2011**, 186, 1455–1461.
- [19] L. X. Hu, F. Yang, W. C. Lu, Y. Hao, H. Yuan, *Appl. Catal. B*, **2013**,

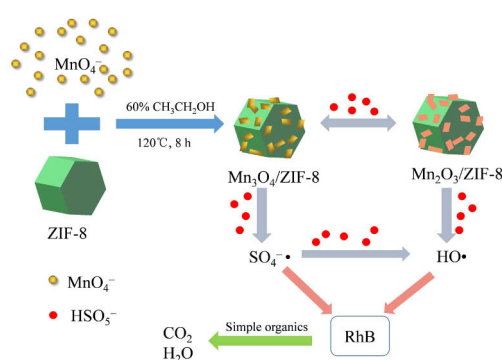
### Graphical Abstract

*Chin. J. Catal.*, 2017, 38: 1360–1372 doi: 10.1016/S1872-2067(17)62875-4

#### Peroxymonosulfate activation by $\text{Mn}_3\text{O}_4$ /metal-organic framework for degradation of refractory aqueous organic pollutant rhodamine B

Longxing Hu\*, Guihua Deng, Wencong Lu, Yongsheng Lu, Yuyao Zhang  
Shanghai University

The catalyst  $\text{Mn}_3\text{O}_4$ /ZIF-8 was synthesized using a facile solvothermal method and used to activate peroxymonosulfate for degradation of the refractory organic dye rhodamine B.



- 134–135, 7–18.
- [20] Q. J. Yang, H. Choi, S. R. Al-Abed, D. D. Dionysiou, *Appl. Catal. B*, **2009**, 88, 462–469.
- [21] C. D. Qi, X. T. Liu, J. Ma, C. Y. Lin, X. W. Li, H. J. Zhang, *Chemosphere*, **2016**, 151, 280–288.
- [22] H. X. Li, J. Q. Wan, Y. W. Ma, Y. Wang, X. Chen, Z. G. Guan, *J. Hazard. Mater.*, **2016**, 318, 154–163.
- [23] Z. L. Chen, S. H. Chen, Y. H. Li, X. L. Si, J. Huang, S. Massey, G. L. Chen, *Mater. Res. Bull.*, **2014**, 57, 170–176.
- [24] F. Ghanbari, M. Moradi, M. Manshour, *J. Environ. Chem. Eng.*, **2014**, 2, 1846–1851.
- [25] I. Arslan-Alaton, T. Olmez-Hanci, S. Khowei, H. Fakhri, *Catal. Today*, **2017**, 280, 199–207.
- [26] H. Q. Sun, Y. X. Wang, S. Z. Liu, L. Ge, L. Wang, Z. H. Zhu, S. B. Wang, *Chem. Commun.*, **2013**, 49, 9914–9916.
- [27] G. P. Anipsitakis, D. D. Dionysiou, *Environ. Sci. Technol.*, **2004**, 38, 3705–3712.
- [28] H. Q. Sun, S. Z. Liu, G. L. Zhou, H. M. Ang, M. O. Tade, S. B. Wang, *ACS Appl. Mater. Interfaces*, **2012**, 4, 5466–5471.
- [29] Z. H. Ai, L. Z. Zhang, F. H. Kong, H. Liu, W. T. Xing, J. R. Qiu, *Mater. Chem. Phys.*, **2008**, 111, 162–167.
- [30] G. S. Cao, L. Su, X. J. Zhang, H. Li, *Mater. Res. Bull.*, **2010**, 45, 425–428.
- [31] M. Yang, D. X. Li, T. Zhao, J. Ma, *J. Disper. Sci. Technol.*, **2010**, 31, 563–566.
- [32] M. Baldi, E. Finocchio, F. Milella, G. Busca, *Appl. Catal. B*, **1998**, 16, 43–51.
- [33] M. I. Zaki, M. A. Hasan, L. Pasupulety, *Appl. Catal. A*, **2000**, 198, 247–259.
- [34] D. L. Zhao, X. Yang, H. Zhang, C. L. Chen, X. K. Wang, *Chem. Eng. J.*, **2010**, 164, 49–55.
- [35] T. A. Saleh, S. Agarwal, V. K. Gupta, *Appl. Catal. B*, **2011**, 106, 46–53.
- [36] S. Lee, B. Choi, N. Hamasuna, C. Fushimi, A. Tsutsumi, *J. Power Sources*, **2008**, 181, 177–181.
- [37] B. Choi, S. Lee, C. Fushimi, A. Tsutsumi, *Electrochim. Acta*, **2011**, 56, 6696–6701.
- [38] M. Fang, X. L. Tan, M. Liu, S. H. Kang, X. Y. Hu, L. D. Zhang, *CrystEngComm*, **2011**, 13, 4915–4920.
- [39] E. Saputra, S. Muhammad, H. Sun, H. M. Ang, M. O. Tade, S. Wang, *Appl. Catal. B*, **2013**, 142–143, 729–735.
- [40] Y. F. Han, F. X. Chen, K. Ramesh, Z. Y. Zhong, E. Widjaja, L. W. Chen, *Appl. Catal. B*, **2007**, 76, 227–234.
- [41] Y. J. Yao, C. Xu, S. M. Yu, D. W. Zhang, S. B. Wang, *Ind. Eng. Chem. Res.*, **2013**, 52, 3637–3645.
- [42] Y. Q. Li, J. Y. Qu, F. Gao, S. Y. Lv, L. Shi, C. X. He, J. C. Sun, *Appl. Catal. B*, **2015**, 162, 268–274.
- [43] J. Y. Qu, L. Shi, C. X. He, F. Gao, B. B. Li, Q. Zhou, H. Hu, G. H. Shao, X. Z. Wang, J. S. Qiu, *Carbon*, **2014**, 66, 485–492.
- [44] L. Yang, C. Hu, Y. L. Nie, J. H. Qu, *Environ. Sci. Technol.*, **2009**, 43, 2525–2529.
- [45] F. Jiao, H. Frei, *Chem. Commun.*, **2010**, 46, 2920–2922.
- [46] S. T. Xing, C. Hu, J. H. Qu, H. He, M. Yang, *Environ. Sci. Technol.*, **2008**, 42, 3363–3368.
- [47] H. Zhao, H. J. Cui, M. L. Fu, *RSC Adv.*, **2014**, 4, 39472–39475.
- [48] D. Y. Zhao, Q. Hao, C. X. Xu, *Electrochim. Acta*, **2015**, 180, 493–500.
- [49] S. B. Khan, M. M. Rahman, H. M. Marwani, A. M. Asiri, K. A. Alamry, M. A. Rub, *Appl. Surf. Sci.*, **2013**, 282, 46–51.
- [50] J. Y. Lee, O. K. Farha, J. Roberts, K. A. Scheidt, S. B. T. Nguyen, J. T. Hupp, *Chem. Soc. Rev.*, **2009**, 38, 1450–1459.
- [51] D. Farrusseng, S. Aguado, C. Pinel, *Angew. Chem. Int. Ed.*, **2009**, 48, 7502–7513.
- [52] Z. Y. Gu, J. Park, A. Raiff, Z. W. Wei, H. C. Zhou, *ChemCatChem*, **2014**, 6, 67–75.
- [53] A. Phan, C. J. Doonan, F. J. Uribe-Romo, C. B. Knobler, M. O’Keeffe, O. M. Yaghi, *Acc. Chem. Res.*, **2010**, 43, 58–67.
- [54] K. S. Park, Z. Ni, A. P. Cote, J. Y. Choi, R. Huang, F. J. Uribe-Romo, H. K. Chae, M. O’Keeffe, O. M. Yaghi, *Proc. Natl. Acad. Sci. USA*, **2006**, 103, 10186–10191.
- [55] Y. F. Han, F. X. Chen, Z. Y. Zhong, K. Ramesh, E. Widjaja, L. W. Chen, *Catal. Commun.*, **2006**, 7, 739–744.
- [56] K. Y. A. Lin, H. A. Chang, *J. Taiwan Inst. Chem. Eng.*, **2015**, 53, 40–45.
- [57] K. Y. Lin, H. A. Chang, R. C. Chen, *Chemosphere*, **2015**, 130, 66–72.
- [58] K. Y. Andrew Lin, F. K. Hsu, W. D. Lee, *J. Mater. Chem. A*, **2015**, 3, 9480–9490.
- [59] K. Y. Lin, B. C. Chen, *Dalton Trans.*, **2016**, 45, 3541–3551.
- [60] S. R. Venna, J. B. Jasinski, M. A. Carreon, *J. Am. Chem. Soc.*, **2010**, 132, 18030–18033.
- [61] H. L. Jiang, T. Akita, T. Ishida, M. Haruta, Q. Xu, *J. Am. Chem. Soc.*, **2011**, 133, 1304–1306.
- [62] Y. A. Zhao, M. M. Liu, B. B. Fan, Y. F. Chen, W. M. Lv, N. Y. Lu, R. F. Li, *Catal. Commun.*, **2014**, 57, 119–123.
- [63] M. M. Liu, B. B. Fan, X. F. Shi, R. F. Li, *Catal. Commun.*, **2013**, 42, 20–24.
- [64] B. Yu, F. F. Wang, W. B. Dong, J. Hou, P. C. Lu, J. B. Gong, *Mater. Lett.*, **2015**, 156, 50–53.
- [65] R. Chandra, S. Mukhopadhyay, M. Nath, *Mater. Lett.*, **2016**, 164, 571–574.
- [66] R. Jain, M. Mathur, S. Sikarwar, A. Mittal, *J. Environ. Manage.*, **2007**, 85, 956–964.
- [67] C. Tatebe, X. Zhong, T. Ohtsuki, H. Kubota, K. Sato, H. Akiyama, *Food Sci. Nutr.*, **2014**, 2, 547–556.
- [68] L. X. Hu, F. Y. Chen, P. F. Hu, L. P. Zou and X. Hu, *J. Mol. Catal. A*, **2016**, 411, 203–213.
- [69] C. P. Bai, W. Q. Gong, D. X. Feng, M. Xian, Q. Zhou, S. H. Chen, Z. X. Ge, Y. S. Zhou, *Chem. Eng. J.*, **2012**, 197, 306–313.
- [70] M. Zhou, H. Yang, T. Xian, R. S. Li, H. M. Zhang, X. X. Wang, *J. Hazard. Mater.*, **2015**, 289, 149–157.
- [71] C. P. Bai, X. F. Xiong, W. Q. Gong, D. X. Feng, M. Xian, Z. X. Ge, N. Xu, *Desalination*, **2011**, 278, 84–90.
- [72] X. Y. Li, Y. Wu, W. Zhu, F. Q. Xue, Y. Qian, C. N. Wang, *Electrochim. Acta*, **2016**, 220, 276–284.
- [73] E. L. Bustamante, J. L. Fernandez and J. M. Zamaro, *J. Colloid Interface Sci.*, **2014**, 424, 37–43.
- [74] F. Cacho-Bailo, B. Seoane, C. Téllez, J. Coronas, *J. Membrane Sci.*, **2014**, 464, 119–126.
- [75] C. H. Wang, C. Liu, J. S. Li, X. Y. Sun, J. Y. Shen, W. Q. Han, L. J. Wang, *Chem. Commun.*, **2017**, 53, 1751–1754.
- [76] M. Shah, H. T. Kwon, V. Tran, S. Sachdeva, H. K. Jeong, *Microporous Mesoporous Mater.*, **2013**, 165, 63–69.
- [77] W. X. Zhang, Z. H. Yang, Y. Liu, S. P. Tang, X. Z. Han and M. Chen, *J. Cryst. Growth*, **2004**, 263, 394–399.
- [78] A. Moses Ezhil Raj, S. G. Victoria, V. B. Jothy, C. Ravidhas, J. Wollschläger, M. Suendorf, M. Neumann, M. Jayachandran, C. Sanjeeviraja, *Appl. Surf. Sci.*, **2010**, 256, 2920–2926.
- [79] R. L. Papporello, E. E. Miró, J. M. Zamaro, *Microporous Mesoporous Mater.*, **2015**, 211, 64–72.
- [80] T. L. Barr, S. Seal, *J. Vac. Sci. Technol. A*, **1995**, 13, 1239–1246.
- [81] F. Y. Tian, A. M. Cerro, A. M. Mosier, H. K. Wayment-Steele, R. S. Shine, A. Park, E. R. Webster, L. E. Johnson, M. S. Johal, L. Benz, *J. Phys. Chem. C*, **2014**, 118, 14449–14456.
- [82] R. Dedryvère, L. Gireaud, S. Grugeon, S. Laruelle, J. M. Tarascon, D. Gonbeau, *J. Phys. Chem. B*, **2005**, 109, 15868–15875.

- [83] H. Chen, L. F. Wang, J. Yang, R. T. Yang, *J. Phys. Chem. C*, **2013**, 117, 7565–7576.
- [84] Y. Hu, H. Kazemian, S. Rohani, Y. Huang, Y. Song, *Chem. Commun.*, **2011**, 47, 12694–12696.
- [85] M. C. McCarthy, V. Varela-Guerrero, G. V. Barnett, H. K. Jeong, *Langmuir*, **2010**, 26, 14636–14641.
- [86] W. X. Zhang, C. Wang, X. M. Zhang, Y. Xie, Y. T. Qian, *Solid State Ionics*, **1999**, 117, 331–335.
- [87] H. W. Liang, H. Q. Sun, A. Patel, P. Shukla, Z. H. Zhu, S. B. Wang, *Appl. Catal. B*, **2012**, 127, 330–335.
- [88] E. Saputra, S. Muhammad, H. Sun, H. M. Ang, M. O. Tadé, S. Wang, *J. Colloid Interface Sci.*, **2013**, 407, 467–473.
- [89] E. Saputra, S. Muhammad, H. Sun, H. M. Ang, M. O. Tadé, S. Wang, *Appl. Catal. B*, **2014**, 154–155, 246–251.
- [90] Y. J. Yao, Y. M. Cai, G. D. Wu, F. Y. Wei, X. Y. Li, H. Chen, S. B. Wang, *J. Hazard. Mater.*, **2015**, 296, 128–137.
- [91] Y. X. Wang, H. Q. Sun, H. M. Ang, M. O. Tadé, S. B. Wang, *J. Colloid Interface Sci.*, **2014**, 433, 68–75.
- [92] Y. X. Wang, H. Q. Sun, H. M. Ang, M. O. Tadé, S. B. Wang, *Appl. Catal. B*, **2015**, 164, 159–167.
- [93] P. Shukla, S. Wang, K. Singh, H. M. Ang, M. O. Tadé, *Appl. Catal. B*, **2010**, 99, 163–169.
- [94] J. Y. Zhao, Y. B. Zhang, X. Quan, S. Chen, *Sep. Purif. Technol.*, **2010**, 71, 302–307.
- [95] J. P. Li, X. Zhang, Z. H. Ai, F. L. Jia, L. Z. Zhang, J. Lin, *J. Phys. Chem. C*, **2007**, 111, 6832–6836.
- [96] F. L. Zhang, J. C. Zhao, L. Zang, T. Shen, H. Hidaka, E. Pelizzetti, N. Serpone, *J. Mol. Catal. A*, **1997**, 120, 173–178.
- [97] Y. X. Wang, S. Indrawirawan, X. G. Duan, H. Q. Sun, H. M. Ang, M. O. Tadé, S. Wang, *Chem. Eng. J.*, **2015**, 266, 12–20.

## Mn<sub>3</sub>O<sub>4</sub>/金属有机骨架材料活化过一硫酸盐降解水中难降解有机污染物罗丹明B

胡龙兴<sup>a,\*</sup>, 邓桂花<sup>a</sup>, 陆文聪<sup>b</sup>, 陆永生<sup>a</sup>, 张雨瑶<sup>a</sup>

<sup>a</sup>上海大学环境与化学工程学院, 上海200444

<sup>b</sup>上海大学理学院, 上海200444

**摘要:** 锰氧化物是一类环境友好型材料, 可以有效活化过一硫酸盐(PMS)降解水中难降解有机污染物。但是锰氧化物在单独使用时容易出现严重的团聚现象, 进而降低其对PMS的催化活性, 不利于水中污染物的降解。因此, 人们通常将锰氧化物负载于多孔的载体材料上。金属有机骨架材料(MOFs)因具有巨大的比表面积和温和的制备条件而广受关注。本文采用温和的溶剂热法首次成功制备了Mn<sub>3</sub>O<sub>4</sub>与MOF的复合材料Mn<sub>3</sub>O<sub>4</sub>/ZIF-8, 并通过X射线衍射、扫描电镜、透射电镜、X射线光电子能谱和红外光谱等手段对其进行了表征, 探究了Mn<sub>3</sub>O<sub>4</sub>/ZIF-8的形成机理。考察了Mn<sub>3</sub>O<sub>4</sub>负载量对Mn<sub>3</sub>O<sub>4</sub>/ZIF-8催化性能的影响, 以及Mn<sub>3</sub>O<sub>4</sub>/ZIF-8投加量、PMS投加量、初始罗丹明B (RhB)浓度和反应温度对RhB去除效果的影响, 同时探究了Mn<sub>3</sub>O<sub>4</sub>/ZIF-8的重复使用性能, 分析了RhB的降解途径、去除机理以及最终的降解副产物。结果表明, 边长为50–150 nm的片状Mn<sub>3</sub>O<sub>4</sub>均匀分散在粒径为250 nm的六边形ZIF-8的外表面; 当Mn<sub>3</sub>O<sub>4</sub>负载量为0.5时, 所制备的复合材料0.5-Mn/ZIF-120活化PMS对RhB的降解效果最好, 反应60 min时RhB降解率可达到99.4%, 且Mn的浸出量可以忽略不计。在该体系中, RhB的降解过程符合一级动力学反应方程, 其降解速率常数随催化剂和PMS投加量的增加、反应温度的提高和初始RhB浓度的减小而增大。在0.5-Mn/ZIF-120催化剂投加量为0.4 g/L、PMS投加量为0.3 g/L、初始RhB浓度为10 mg/L、初始溶液pH为5.18及室温(23 °C)条件下, 水中RhB的降解率在40 min时即可达到98%。淬灭实验表明, 该体系中HO•起主导作用, 而其主要来源于活化PMS所产生的SO<sub>4</sub>•<sup>-</sup>。此外, 通过简单的二次水冲洗方式对0.5-Mn/ZIF-120催化剂进行回收使用, 在连续5次循环使用后仍然可见较高的催化活性和稳定性, RhB的去除率保持在96%以上, 且Mn的浸出百分率始终低于5%。

**关键词:** 过一硫酸盐活化; 难降解有机污染物; 降解; 金属有机骨架材料; Mn<sub>3</sub>O<sub>4</sub>/ZIF-8

收稿日期: 2017-04-26. 接受日期: 2017-06-19. 出版日期: 2017-08-05.

\*通讯联系人. 电话/传真: (021)66137771; 电子邮箱: hulxh@shu.edu.cn

基金来源: 国家重点研究发展计划(2016YFB0700504).

本文的英文电子版由Elsevier出版社在ScienceDirect上出版(<http://www.sciencedirect.com/science/journal/18722067>).